GEOLOGY

The role of iron-rich hydrosaline liquids in the formation of Kiruna-type iron oxide–apatite deposits

Li-Ping Zeng[1], Xin-Fu Zhao[1]*, Carl Spandler[2], John A. Mavrogenes[3], Terrence P. Mernagh[3], Wang Liao[1], Yi-Zhe Fan[1], Yi Hu[4], Bin Fu[3], Jian-Wei Li[1]

Kiruna-type iron oxide–apatite (IOA) deposits, an important source of iron, show close associations with andesitic subvolcanic intrusions. However, the processes of ore formation and the mechanism controlling iron concentration remain uncertain. Here, we report the widespread presence of high-temperature (>800°C) water-poor multisolid hydrosaline liquid inclusions in pre- and syn-ore minerals from IOA deposits of eastern China. These inclusions consistently homogenize to a liquid phase by vapor disappearance and mostly contain 3 to 10 wt % Fe, signifying a substantial capacity for iron transportation by such hydrosaline liquids. We propose that the hydrosaline liquids were likely immiscible from the dioritic magmas with high Cl/H_2O in subvolcanic settings. Subsequent reaction with host rocks and/or decompression and cooling of the hydrosaline liquids is deemed responsible for the simultaneous formation of high-temperature alteration and magnetite ores, thereby providing important insights into the distinctive characteristics of IOA deposits in shallow magmatic-hydrothermal systems.

INTRODUCTION

Kiruna-type iron oxide–apatite (IOA) deposits, an important global resource of iron and potentially rare earth elements (REEs) and phosphorus, consist of massive, disseminated, brecciated, and/or vein-type magnetite + apatite + diopside and/or actinolite ores (*1*–*6*). It has long been recognized that IOA deposits are spatially and temporally associated with subvolcanic intrusions and/or volcanic rocks and formed under high-temperature (up to ~900°C) and low-pressure (as low as 10 MPa) conditions (*1*–*10*). An enigmatic aspect of this deposit type is the extensive high-temperature sodic alteration halos around the orebodies, which may also contain lava-like ore structures and high-Ti (>1 wt %) magnetite with ilmenite lamellae, features typically considered to be of igneous origin (*11*–*17*). A range of genetic models have been proposed, including iron oxide or sulfate (±carbonate) melts formed via magma immiscibility, flotation of igneous magnetite micro-aggregates, and replacement by magmatic hydrothermal fluids (*1*–*4*, *8*–*14*, *18*–*22*). Recent research has focused on high-temperature melt/fluid inclusions as these provide critical clues for understanding the nature and origin of the initial ore-forming fluids/liquids or iron-rich melts (*8*, *9*, *21*–*25*).

Volatile phases exsolved from magmas are an important agent for transport and accumulation of metals in intrusion-related ore systems. In shallow subvolcanic settings, experimental data and observations of natural samples support the premise that high-salinity liquids (hereafter referred to as hydrosaline liquids) can form through immiscibility from high Cl/H_2O silicate melts or by vapor-liquid (brine) unmixing of magmatic fluids (*26*–*29*). Hydrosaline liquid is used to describe magmatic highly saline liquids with ≥42 wt % $NaCl_{equiv.}$ and shows physicochemical properties distinct from those of H_2O-dominant aqueous fluids (*28*, *30*, *31*). Evidence for hydrosaline liquids is typically preserved as multiphase inclusions in various deposit types formed in shallow magmatic-hydrothermal environments, including porphyry gold, porphyry copper ± gold, skarn, granite-related tin-tungsten, and IOA deposits, and occasionally within quartz and miarolitic cavities of igneous rocks (*23*, *30*, *32*–*36*). These inclusions often contain multiple daughter mineral phases (e.g., halite + sylvite ± sulfates ± carbonates ± fluorite ± sulfides ± oxides) and a minor liquid phase. Heating experiments reveal they reach total homogenization (i.e., complete solid dissolution and/or fluid miscibility into a single liquid phase) mostly >600°C (*33*–*36*), which are interpreted to record the temperatures of fluid/liquid entrapment. Beyond this, the origin of hydrosaline liquids and their roles in ore formation remain poorly understood.

The Ningwu and Luzong volcanic fields of the Middle and Lower Yangtze River Metallogenic Belt, eastern China, host >40 known IOA deposits with a total resource of >3200 million tons (Mt) of Fe-oxides (*1*, *3*, *4*, *37*, *38*). Most of these deposits formed at ~130 million years ago and show close spatial and temporal associations with alkali rich ($Na_2O + K_2O$ = 5 to 9 wt %) dioritic porphyry intrusions emplaced at depths ≤2 km (*1*, *3*, *4*, *37*–*39*). In this contribution, we document high-temperature hydrosaline liquid inclusions (HLIs) widely observed within pre- and syn-ore alteration minerals (metasomatic zircon, diopside, garnet, and magnetite) in these IOA deposits. High contents of iron have been measured in the primary HLIs using laser ablation inductively coupled plasma mass spectrometry (LA-ICP-MS), highlighting the substantial capacities of these liquids for transporting iron. This study provides important insights into the nature and origin of initial ore-forming liquids and allows us to propose a genetic model for the formation of Kiruna-type IOA deposits.

RESULTS

Geological setting

This work focuses on analyzing fluid inclusions from the most representative IOA deposits in the Ningwu and Luzong volcanic fields, including the Taocun, Meishan, and Luohe deposits. In general, the orebodies of these IOA deposits are mainly hosted along contacts between the dioritic porphyry intrusions and the overlying Cretaceous volcanic rocks or within the volcanic rocks (figs. S1 and S3) (*1*,

[1]State Key Laboratory of Geological Processes and Mineral Resources, and School of Earth Resources, China University of Geosciences, Wuhan, Hubei, China. [2]Department of Earth Sciences, The University of Adelaide, Adelaide, South Australia, Australia. [3]Research School of Earth Sciences, Australian National University, Canberra, ACT, Australia. [4]Advanced Analytical Center, James Cook University, Townsville, Queensland, Australia.
*Corresponding author. Email: xfzhao@cug.edu.cn

3, *4*). The IOA orebodies commonly exhibit stratiform or lens-shaped geometries and occasionally show domelike shapes within breccia bodies.

In general, these deposits were affected by three stages of alteration and mineralization, as follows: pre-ore Na stage (I), syn-ore (Na)-Fe-Ca stage (II), and post-ore Ca-Mg stage (III) (figs. S1 and S2) (*1*, *3*, *4*, *39*). Stage I Na alteration is extensive and mostly developed within the uppermost parts of the ore-hosting intrusions and the surrounding volcanic rocks. It is characterized by variable proportions of albite and scapolite locally with minor tourmaline, forming albitite zones enveloping the magnetite orebodies. Stage II (Na)-Ca-Fe alteration overprints the sodic alteration zones and contains high-Ti magnetite with ilmenite lamellae coexisting with variable proportions of fluorapatite, diopside, garnet, and actinolite. Stage III mineral assemblages are marked by intense chlorite-epidote-pyrite-hematite-quartz-(chalcopyrite) alteration. The observed alteration sequences are consistent with IOA deposits worldwide (*5*–*7*, *14*).

A total of 10 samples were selected for HLIs measurements, comprising four samples of albitized host rocks representing the stage I Na alteration and six samples from stage II (Na)-Ca-Fe alteration. Detailed descriptions of the geology of each deposit and samples are available in the Supplementary Materials.

Petrography, microthermometry, and LA-ICP-MS analysis of HLIs

Both stages I and II alteration minerals (diopside, garnet, and metasomatic zircon) commonly contain HLIs, mainly consisting of 70 to 90 vol % multiphase solids and a vapor bubble of 10 to 30 vol % (Figs. 1 and 2). Most of these HLIs range in size from 5 to 65 μm. They occur either as clusters along mineral growth zones or as isolated individual

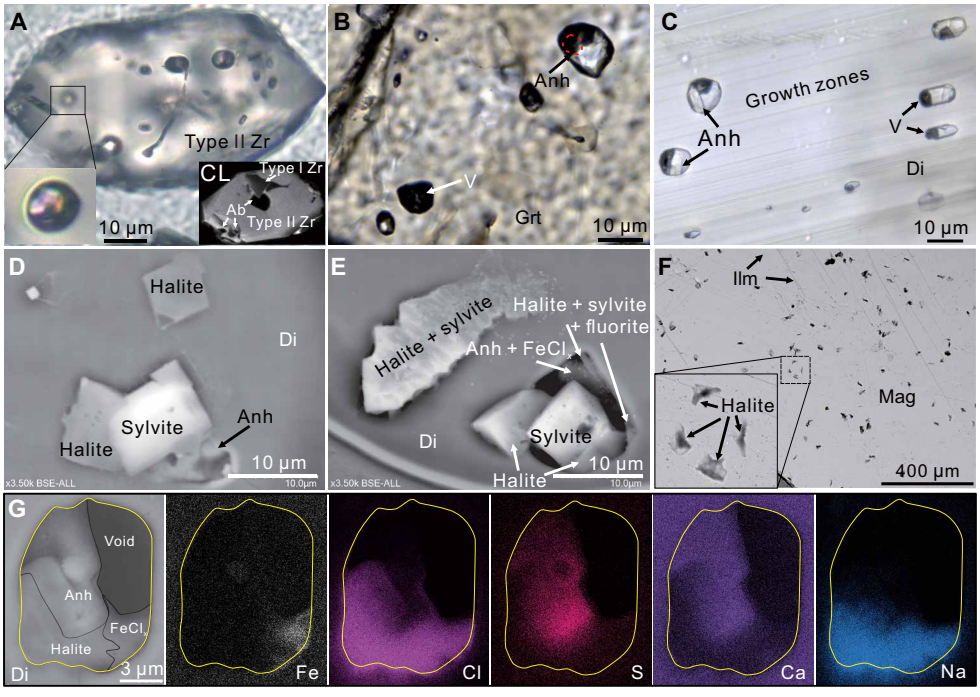

Fig. 1. Images and analyses of the HLIs in pre- to syn-ore minerals. (**A**) Coeval albite (Ab) and HLIs entrapped within type II zircon (Zr) domain. The inset showing the same Zr grain under cathodoluminescence (CL) image. (**B**) Garnet (Grt) with a boiling assemblage of hydrosaline liquid and vapor (V) inclusions. The HLI (in the upper right) that contains an anhydrite crystal (marked by dotted red circle), which corresponds to the Raman spectra, is shown in fig. S8A. (**C**) An assemblage of HLIs hosted within growth zones of diopside, indicating a primary origin. (**D** to **G**) Backscattered electron images and element maps of exposed inclusions within diopside (Di) and primary magnetite (Mag) with ilmenite (Ilm) lamella. The HLIs contain daughter minerals of halite, sylvite, Fe-chlorides, anhydrite, and fluorite.

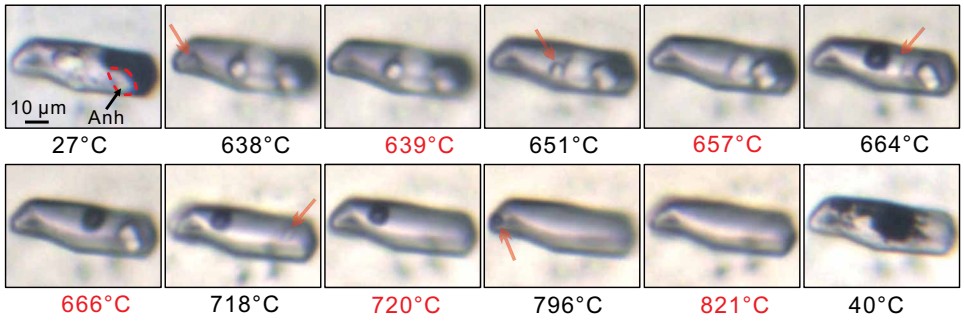

Fig. 2. Behavior of an HLI hosted within diopside upon heating. Solid crystal dissolved sequentially at 639°C, followed by 657°, 666°, and 720°C (for anhydrite). Total homogenization to the liquid phase by vapor disappearance occurred at 821°C. After cooling to room temperature, all the daughter minerals recrystallized, and the bubble reappeared.

inclusions (Fig. 1 and figs. S3 and S5), attesting to their primary origin (*26*, *40*). Pseudo-secondary inclusions are also locally present along the healed fractures and show similar phase proportions to those in the primary inclusions. Although no aqueous liquid is observed at room temperature, interstitial H_2O phases were detected by Raman spectroscopy (fig. S8B). Most vapor phases within the inclusions have no Raman-active vibrations (fig. S8A), while a few have Raman peaks consistent with CO_2 and SO_2 (*23*). The inclusions commonly contain abundant transparent daughter minerals, including halite + sylvite (~20 to 60 vol %), anhydrite (<~40 vol %), Fe-chlorides, and possibly minor barite as well as fluorite, as identified by Raman spectroscopy and scanning electron microscope–energy-dispersive x-ray spectroscopy (SEM-EDS) on exposed inclusions (Figs. 1 and 2). In addition, they occasionally contain opaque minerals, including reddish hematite (fig. S3C) and/or pyrite. Locally, these HLIs coexist with low-density vapor inclusions (Fig. 1B and fig. S3I), which may contain minor H_2O, CO_2, and SO_2 phases (*23*). The HLIs are also identified within primary magnetite grains characterized by ilmenite lamellae (Fig. 1F). The HLIs vary size ranging from 5 to 40 μm, occur as clusters or along pseudosecondary trails, and also contain multi-daughter phases (halite, sylvite, anhydrite, and Mg-chloride), as revealed by SEM-EDS.

Microthermometric measurements were conducted on the HLI assemblages hosted within diopside and garnet (table S2). Inclusions with postentrapment modification features, such as necking or decrepitation, were excluded from subsequent analysis and discussion. The inclusions within metasomatic zircons contain daughter minerals and phase proportions similar to those hosted within diopside and garnet, likely indicating a comparable origin and homogenization behavior. Total homogenization of the HLIs is defined by vapor disappearance to the liquid phase, as illustrated by a typical heating sequence of an HLI in Fig. 2. The first transparent daughter mineral dissolves above 400°C, commonly ranging from 480° to 650°C. Halite (NaCl) and the last solid phase mineral (commonly anhydrite) disappear at 610° to 733°C and 699° to 762°C, respectively. The homogenization temperatures of 28 measured HLI assemblages range from 787° to 928°C with an average value of 865 ± 29 (1σ) °C (fig. S9), while the maximum variation of total homogenization temperatures within an HLI assemblage is less than 50°C. The corresponding salinities of these HLIs range from 76 to 92 wt % $NaCl_{equiv.}$ calculated from halite final melting temperatures (610° to 733°C) using the equation of the H_2O-NaCl system (*41*). However, considering that many HLIs contain variable anhydrite and an only minor amount of interstitial water, the salinities of many inclusions likely exceed 92 wt % salt and may approach 100 wt % salt.

In situ analysis of the HLIs hosted within metasomatic zircon was performed using LA-ICP-MS, as compositions of the HLIs hosted within diopside and garnet were compromised by the high contents of Fe and Ca in the host minerals (*23*). Assuming a total salinity of 100 wt % salt (see Materials and Methods), the inclusions have elevated concentrations of Na (12 to 22 wt %), K (5 to 13 wt %), Cl (20 to 42 wt %), Fe (0.8 to 10 wt % with an average value of 5 wt %), Ca (2 to 15 wt %), and S (7 to 18 wt %) (Fig. 3 and table S3). They also contain considerable amounts of Ti, Mg, Zn, Rb, Sr, Cs, and Pb, which can range from tens of parts per million (ppm) to several wt %. Although phosphorus is poorly detected by LA-ICP-MS, the transient signals of some spot analyses show an obvious bulge in the P counts during the ablation of the HLIs (Fig. 3), indicating that the hydrosaline liquids can transport some P, which is also consistent with previous studies (*23*).

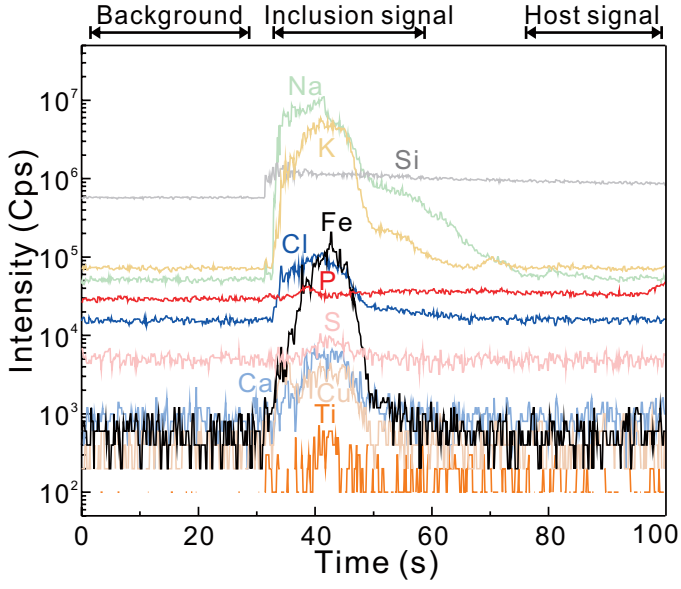

Fig. 3. Representative LA-ICP-MS transient signals of selected elements obtained from an HLI (25 × 28 μm) hosted within metasomatic zircon.

DISCUSSION

Linking metasomatic zircon to ore mineralization of IOA deposits

Metasomatic zircons, showing complex rim-core textures as revealed by cathodoluminescence (CL) images (Fig. 1A and fig. S5), were identified and separated from the albitized intrusive and andesitic rocks in these IOA deposits. These zircon grains contain two types of domains. Type I domains, if present, commonly occur as cores with intermediate CL intensities displaying oscillatory zoning, which is typical of igneous zircon (fig. S5, A, C, and D). Type II domains of zircon have bright CL intensities and occur along grain boundaries and microfractures of type I domains. Type II domains commonly contain abundant albite mineral inclusions in addition to the HLIs (Fig. 1A and fig. S5). The sharp contact and different elemental compositions between the domains of type I and type II zircon indicate that the type II domains were formed from type I zircon via metasomatic process (i.e., metasomatic zircon) (*42*–*44*).

In situ analyses reveal that the type II metasomatic zircon domains have notably lower contents of P, Y, total REEs, U, Th, and Ti, compared to Type I igneous domains (fig. S6 and data S1), implying the leaching of trace elements during metasomatism (*42*). The enclosed HLIs and albite mineral inclusions within domains of metasomatic zircon are the entrapped metasomatic liquids and the reaction products, and both are indicative of sodic alteration (Fig. 1A and fig. S5) (*42*, *44*). In combination, the presence of abundant hydrosaline liquid and albite inclusions within metasomatic zircons indicates that the metasomatic liquids were highly saline and relatively alkaline, as revealed by experimental results of zircon metasomatism (*43*, *44*). Therefore, the formation of metasomatic zircons is coeval with albitization, and the corresponding HLIs hence represent the liquids responsible for albitization, as the earliest ore-forming liquids of the IOA deposits.

Nature and origin of hydrosaline liquid

The HLIs in this study consistently homogenize to a liquid phase, indicating that all the mineral phases crystallized from the trapped liquid. LA-ICP-MS spot analyses reveal Na-K-Fe-Ca-Cl-SO_4 to be the major components, together with considerable Ti contents. The hydrosaline liquids contain high iron contents, up to 10 wt %, indicating that such liquids can transport substantial amounts of iron. Iron chlorides were revealed by SEM-EDS as daughter minerals within the HLIs and a broad positive correlation between Fe and Cl peaks is observed in time-resolved LA-ICP-MS signals (Figs. 1, E and G, and 3), implying that Fe-chlorides are the main iron species in the HLIs. Such observations are consistent with previously high-temperature experimental studies of saline fluids (*45*).

Although the effect of multiple components (Na-K-Fe-Ca-Cl-SO_4) on the pressure-temperature-volume systematics of liquids has not been experimentally evaluated, we interpret the measured homogenization temperatures (787° to 928°C with an average of 865°C) to broadly represent the entrapment temperatures of the hydrosaline liquids. Several lines of evidence support this interpretation: (i) Inclusions within different host minerals show consistent homogenization behaviors and total homogenization temperatures (table S2), suggesting that the effect of nonreversible fluid-host interactions and volatile loss during cooling was negligible (*23*); (ii) the homogenization temperatures align with temperatures estimated based on ilmenite-magnetite geothermometry, magnetite-Mg geothermometry, and two-mineral oxygen isotope geothermometry in the studied deposit (*17*, *46*); and (iii) the temperatures are consistent with ore formation temperatures recently reported for other IOA deposits worldwide (*8*–*10*, *19*, *21*, *27*, *32*). On the basis of the H_2O-NaCl phase diagram, the hydrosaline liquids are stable at temperatures and pressures of subvolcanic settings (Fig. 4), which can be inferred to be similar in the more complicated H_2O-NaCl-KCl-$FeCl_x$-$CaSO_4$ system (*27*, *30*, *33*–*36*).

The HLIs are characterized by high K/Na, Ca/Na, Cs/Na, Rb/Na, Zn/Na, and K/Na but low Ca/K mass ratios, which are similar to those obtained by previous analyses of saline fluid inclusions in intrusion-related porphyry and skarn systems (fig. S10) (*47*, *48*). To further determine the source of hydrosaline liquids, in situ oxygen isotopes were measured on the metasomatic zircon domains using SIMS, yielding $\delta^{18}O$ values of +5.0 to +7.7 per mil (‰; fig. S7 and table S1). The calculated $\delta^{18}O$ values of the hydrosaline liquids coexisting with metasomatic zircons at 865°C range from +6.6 to +9.3‰, which are typical of magmatic fluids (+5.5 to +9.2‰) (*49*, *50*). These findings, together with the published boron isotopes of tourmaline associated with stage I albitization and O-Sr isotopes of magnetite and apatite from ore samples (*39*, *46*, *51*), all support a magmatic origin for the hydrosaline liquids, although a role of the assimilation/dissolution of evaporites is not ruled out (*19*–*23*).

In magmatic-hydrothermal systems, the compositions of volatile phases in equilibrium with silicate melts are mainly controlled by the ratios of Cl relative to H_2O in the melts and the pressure-temperature conditions (*28*, *52*). Experimental studies have shown that hydrosaline liquids can directly exsolve from the dioritic magmas with elevated Cl/H_2O ratios (>0.35) (*28*). Furthermore, high S concentrations in relatively oxidized melts can reduce the solubility of Cl in the melt, thereby decreasing Cl/H_2O ratio required for direct exsolution of hydrosaline liquids from the respective melt, which thus promote the exsolution of SO^{2-}_4-bearing hydrosaline liquids (*53*). In subvolcanic-volcanic settings, the exsolved hydrosaline liquids, if water phases are present, are likely to undergo further unmixing until producing vapor and coexisted water-poor hydrosaline liquids as recorded by inclusions within the earliest alteration minerals. Alternatively, immiscibility of vapor and high-salinity liquids from a single-phase low-salinity fluid (i.e., fluid boiling) has been commonly advocated in porphyry Cu-Au systems at shallow environments (*27*, *33*, *34*, *52*). In this study, vapor inclusions rarely coexist with HLIs and are volumetrically minor compared to the liquid phase, which is inconsistent with the scenario of a predominant role of vapor-liquid immiscibility. Chlorine and H_2O concentrations in magmas associated with IOA deposits have been rarely addressed. However, Watts and Mercer (*24*) reported relatively high Cl (up to 9000 ppm) and low H_2O (<3.2 wt %) contents in trachydacitic to rhyolitic melt inclusions in the Pea Ridge deposit, implying that decompression of such magmas may increase Cl/H_2O ratios to allow direct exsolution of hydrosaline liquids. In addition,

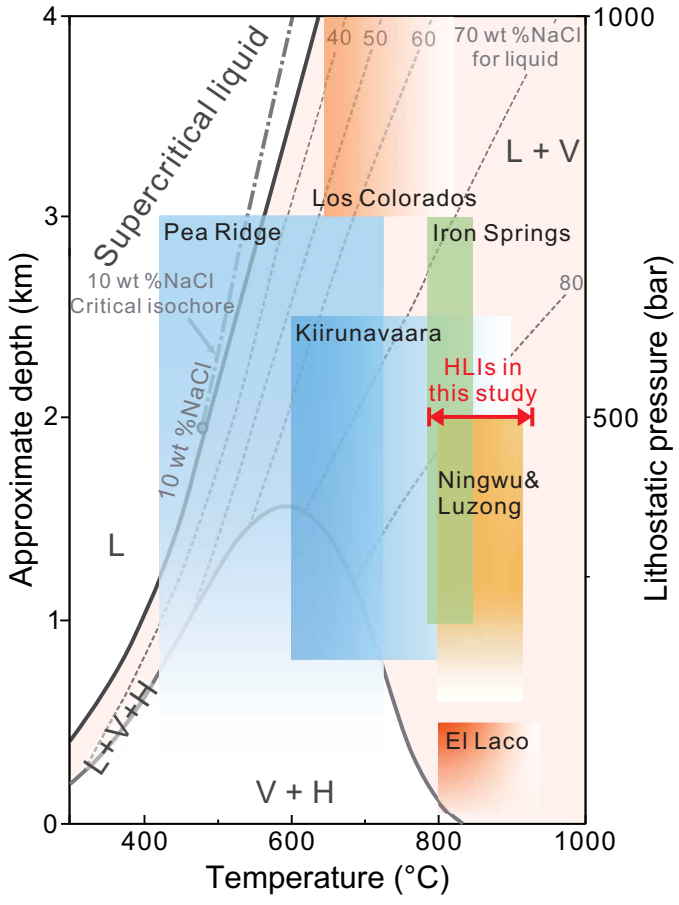

Fig. 4. A compile of depth-temperature data of global IOA deposits illustrating the locations within the stability field of hydrosaline liquids in the H_2O-NaCl system. The formation depths (lithostatic pressures) are estimated from stratigraphic reconstructions, and temperatures of magnetite formation are calculated using oxygen isotopes of mineral pairs and mineral thermometers (table S4). The red double arrow shows the microthermometric temperatures from the HLIs at 500 bar (~2 km) in this study. The light pink area represents the stability field of vapor (V)–liquid (L) immiscibility, and salinities (wt % $NaCl_{equiv.}$) of the liquid are marked by dashed gray lines in the simple H_2O-NaCl system (*27*, *29*). We note that the liquid systems of IOA deposits would be more complex than the H_2O-NaCl system. L + V + H = liquid + vapor + halite; V + H = vapor + halite.

NaCl solid inclusions in dacite glass hosted within plagioclase phenocrysts was reported in the El Laco deposit (*25*), supporting an immiscible origin of salt from silicate magma. We hence speculate that direct exsolution of hydrosaline liquids from high Cl/H_2O dioritic magmas (*28*) is likely dominant in the studied IOA deposits. Such high-Cl/H_2O magmas may be derived from a mantle source metasomatically enriched in NaCl by slab fluids during subduction (*24*, *54*) or formed through assimilation of evaporite-bearing rocks during magma emplacement (*12*, *19*–*23*). However, we note that the proportion of the vapor phases in the studied system may be underestimated, as the conjugated vapor may not be effectively trapped in the host minerals, due to the wetting property of vapor and/or the buoyancy of vapor causing rapid ascent compared to the hydrosaline liquids (*27*, *29*).

An integrated genetic model for IOA deposits and some implications

The close spatial association between orebodies and alteration zones, coupled with the ubiquitous presence of Fe-rich (up to 10 wt %) HLIs in pre- and syn-ore minerals (Fig. 1 and figs. S1 to S3), suggests that such liquids played a key role in efficient iron transport and accumulation in the studied IOA deposits. In such shallow subvolcanic settings, hydrosaline liquids may repeatedly form via direct exsolution from the source dioritic magmas with high Cl/H_2O ratios (Fig. 5). The hydrosaline liquids may have accumulated as transient pools at the apical zones of intrusions or other favorable sites (such as fractures and contact zones between the intrusive porphyry and country rocks), due to the contrasting physical properties (e.g., density and porosity) of the hydrosaline liquids with the surrounding rocks (*55*). Experimental studies have demonstrated that albite and scapolite can be formed by the replacement of feldspar by NaCl ± $CaCl_2$ ± KCl molten salts or by Na-rich chloride fluids at >550°C (*42*, *56*–*59*). The hydrosaline liquids can penetrate and interact with country rocks resulting in the loss of substantial Cl, which then leads to the formation of Fe orebodies and the associated sodic-calcic alteration zones, as observed in the disseminated to the massive ores of this study. Magnetite precipitation from such liquids may also occur as open space filling (e.g., faults and breccias) due to decompression and cooling (*6*), leading to the development of magnetite-rich veins and breccia bodies and even massive ores in sharp contact with the country rocks. Cases where these liquids vent to the surface may also lead to rapid magnetite precipitation, as has been suggested for the El Laco deposit of Chile (*16*).

The proposed model for IOA genesis shows some similarities to previous metasomatic models that invoke Fe transport and precipitation via saline hydrothermal fluids (*1*–*4*, *7*, *12*–*14*), except that the capacity of water-poor hydrosaline liquids to transport and concentrate Fe (and other so-called "fluid immobile" elements such as P and Ti) is substantially enhanced. Considering the high contents of Fe (average of 5 wt %) measured in the studied HLIs, and assuming 90% Fe precipitation efficiency, a volume of 3.8 km^3 (assuming $\rho = 2.1$ g/cm^3 by calculation based on simplified HLIs with 90 vol % daughter minerals composed of 95 wt % NaCl and 5 wt % $FeCl_2$ and 10 vol % vapor phase with a density of 0.001 g/cm^3) of hydrosaline liquid is sufficient to form large iron ore deposits, such as the Luohe (1 Gt ores at 35 wt % Fe) deposit. To exsolve this volume of hydrosaline liquid would require on the order of 270 km^3 volume of dioritic magma (assuming 9000 ppm Cl, 3.4 wt % H_2O, 2.64 g/cm^3 density, and 85% Cl exsolution efficiency) (*24*), which is at the moderate end of the size of plutons emplaced into the crust (*60*), and is consistent with regional geological relationships

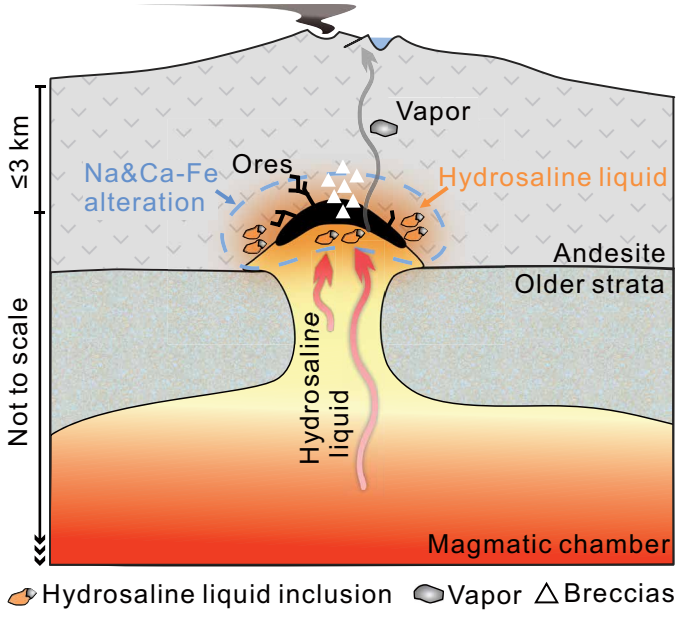

Fig. 5. A schematic diagram illustrating the formation of IOA deposits by high-temperature water-poor and Fe-rich hydrosaline liquids. Hydrosaline liquids, likely formed through directly exsolution from the high-Cl/H_2O dioritic magmas in subvolcanic settings, accumulate in transient pools at the apical zones of the porphyry. Subsequent reaction of these liquids with the surrounding rocks and decompression and cooling forms magnetite orebodies and the associated Na and Ca-Fe alteration.

(*1*, *3*, *4*, *37*, *38*). Besides, the HLIs also contain considerable Ti, P, and F (Figs. 1E and 3), which is also consistent with abundant Ti-rich magnetite and fluorapatite in IOA systems (*13*–*17*). Experimental results and previous studies have revealed that hydrosaline liquids could also transport REEs (*23*, *31*), which are commonly enriched in IOA ores. Hence, high-temperature hydrosaline liquids are not only plausible agents to transport and accumulate iron and other components from the dioritic magmas but can also explain the formation of high-temperature Ti-rich magnetite and the associated alteration phases observed in IOA deposits (*14*–*17*).

Similar HLIs have been also reported within pre- to syn-ore stage alteration minerals and magnetite in other IOA deposits, including the El Laco, Los Colorados, Pea Ridge, Kiirunavaara, Buena Vista, and Iron Springs deposits (*9*, *13*, *19*, *21*–*23*, *32*, *61*), but no consensus on their origins and roles in IOA systems has been reached yet. A compilation of the formation temperatures (estimated from oxygen isotopes of mineral pairs and mineral thermometers) and depths (based on stratigraphic reconstructions) of the prominent IOA deposits globally reveals that most IOA deposits form at shallow levels (≤3 km) and at very high temperatures (>600°C) and all within the stability field of hydrosaline liquids with >70 wt % $NaCl_{equiv.}$ in the H_2O-NaCl system (Fig. 4 and table S4) (*27*, *29*). Furthermore, almost all IOA deposits show temporal, spatial, and genetic associations with subvolcanic intrusions and/or volcanic rocks (*1*–*8*, *11*, *62*), indicating that such a setting is favorable for the formation of high-temperature magmatic hydrosaline liquids. The wide presence of sodic alteration in IOA deposits globally also provides unambiguous evidence for the initial ore-forming liquids being highly saline (table S4) (*12*). The lines of

evidence above suggest that magmatic hydrosaline liquids are common and play an important role in IOA deposits worldwide.

The proposed model of Fe-rich hydrosaline liquids could have implications for other mineralization systems associated with shallow intrusions (*30*, *35*), such as iron skarn and iron oxide-copper-gold deposits, where extensive alkaline alteration and the presence of HLIs have been documented. Many of these deposits (e.g., Olympic Dam, South Australia) represent colossal concentrations of metals that are difficult to reconcile via the actions of hydrothermal fluids alone (*63*). By contrast, the involvement of voluminous hydrosaline liquids, with their superior metal transporting capacity, may provide a viable mechanism to reconcile this quantum of localized metal concentration in the crust. Future investigations to elucidate the physical and chemical details of hydrosaline liquids in a range of settings will likely prove fruitful for developing a comprehensive understanding of ore-forming processes in a range of magmatic-hydrothermal ore systems.

MATERIALS AND METHODS

Descriptions of the studied samples (materials) are available in the Supplementary Materials.

SEM-EDS and SEM-CL

Spot analyses and elemental mapping of EDS were conducted to identify the compositions of solid phases in the exposed HLIs. The inclusions hosted within transparent minerals were exposed via laser ablation with large spot sizes (100 to 150 μm) and relatively low repletion rates of 1 to 2 Hz, while those within the magnetite samples were polished using alcohol on the sandpaper with a grit of 2000 to 9000. To avoid loss of water-soluble components or hydration of phases, the exposed samples were stored in a desiccator and were carried out EDS analyses with gold coating within 2 hours. The SEM-EDS analyses were performed using a Zeiss Sigma 300 field-emission SEM (FE-SEM) equipped with Oxford Instruments X-MaxN EDS system at the Advanced Analytical Centre (AAC), James Cook University (JCU), Australia. The accelerating voltage was set to 20 kV, the working distance was about 7.5 to 8.5 mm, and the spatial resolution was better than 4 nm. In addition, SEM-CL images were also acquired at AAC, JCU using a FE-SEM equipped with panchromatic CL detectors.

Raman spectroscopy

Raman analyses of daughter minerals in individual HLIs were conducted by a WITec Alpha Access 300 instrument coupled with a modified Zeiss microscope with a 100× objective at the AAC, JCU. The Ar + laser wavelength was 532 nm, the diameter of the laser beam was <1 μm, the acquisition time was 30 to 60 s for each analysis with two accumulations, and the spectrometer resolution was 1 cm^{-1}. Data were processed via the WITec Project Data Analysis Software 4.1, and spectral interpretation relied on the RRUFF database (https://rruff.info/).

Microthermometry of HLIs

Microthermometric analyses of high-temperature HLIs were carried out using a Linkam TS1400XY heating stage (up to ~1200°C) at the Research School of Earth Sciences (RSES), the Australian National University (ANU), Australia. The temperature was calibrated at the melting points of NaCl (800.7°C) and gold (1064.4°C) with the estimated accuracy of ±5°C. The heating rate applied was 20°C per minute, which was subsequently reduced to 1° to 2°C per minute when approaching the phase changes (*36*).

LA-ICP-MS measurements of zircon and individual inclusions

In situ analyses of zircon and individual HLIs were conducted using a Teledyne Analyte G2 193 nm ArF excimer laser ablation system connected to a Thermo iCAP-RQ ICP-MS at AAC, JCU. The LA system was equipped with a HelEx II 2-volume ablation chamber. Helium was used as the carrier gas in the ablation chamber and was mixed with Ar via a three-way mixing bulb (volume ~ 5 cm^3) before introduction to the ICP to obtain smooth signals (*64*). The laser was operated with a laser energy density of 3 J/cm^2 and repletion rates of 5 Hz. For analyses of zircon, the beam diameter was conducted at 50 μm. Data acquisition of each analysis consisted of 30 s of background measurement followed by 40 s of sample analysis during ablation. The elements measured include ^{23}Na, ^{27}Al, ^{29}Si, ^{31}P, ^{44}Ca, ^{49}Ti, ^{51}V, ^{55}Mn, ^{88}Sr, ^{89}Y, ^{93}Nb, ^{121}Sb, ^{139}La, ^{140}Ce, ^{141}Pr, ^{143}Nd, ^{147}Sm, ^{151}Eu, ^{143}Nd, ^{147}Sm, ^{157}Gd, ^{159}Tb, ^{163}Dy, ^{165}Ho, ^{167}Er, ^{169}Tm, ^{171}Yd, ^{175}Lu, ^{178}Hf, ^{181}Ta, ^{204}Pb, ^{206}Pb, ^{207}Pb, ^{208}Pb, ^{232}Th, and ^{238}U. Electron microprobe analyses revealed that the Zr contents in type I and type II domains of zircon range from 47.42 to 48.87 wt % (48.01 ± 0.47 wt %, 1σ, $n = 10$) and 47.30 to 49.32 wt % (48.20 ± 0.71 wt %, 1σ, $n = 11$), respectively. The average values of Si content of two types zircon domains were used as the internal standard for the respective zircon domain. The Iolite software package was used for LA-ICP-MS data reduction (*65*). Signals were calibrated using USGS GS-series GSD-1g basaltic glass. GSE-1g basaltic glass, NIST-610 glass and NIST-612 glass were used as secondary standards for all elements. Selected trace element contents of 17 spot analyses on NIST-610 and NIST-612 in this study had a small variation (mostly <10%) compared to those recommendation values (data S1). Relative precision for trace elements of zircon is typically better than ±10%.

For analyses of single HLI, the beam diameter was set to between 20 to 45 μm depending on the sizes of the inclusions. Both individual HLIs and the hosting metasomatic zircon were ablated together, and the contributions from the co-ablated host were subtracted numerically by assuming silicon was present only in the host (zircon). An average value of Si content (15.18 ± 0.29 wt %, 1σ, $n = 11$) for type II domains of zircon is used as the internal standard for calibration of elemental compositions of zircon host mineral. Scapolite standard BB1 was used as an external standard for Cl and Br data reduction (*64*, *66*). In-house scapolite standard Bellin has higher S contents (13,830 ± 540 ppm) than BB1 and was thus used to quantify the S concentrations of the unknown samples. SY scapolite was measured as an unknown to monitor the accuracy of Cl and Br contents. All other trace elements were reduced via the software package SILLS with GSD-1g basaltic glass analyzed as the primary calibration standard, and GSE-1g basaltic glass and the NIST SRM 610 and 612 glasses analyzed as secondary standards to monitor accuracy (*67*). The obtained contents of Cl and S of eight spot analyses on the SY scapolite standard have 0.4 and 4% relative difference, respectively, compared to recommended values (data S2) (*64*, *66*). Selected element concentrations of nine spot analyses on GSD-1g obtained by this study had variations of less than 5% compared to the recommended values, except for phosphorus with 37% (data S2). Combined with uncertainties from potential matrix effects (~5 to 15%), the total uncertainty could be ~10 to 35%. Considering minor water, we quantify the concentration of the major cations (Na^+, K^+, Ca^{2+}, and $Fe^{2+?}$) and anions (Cl^- and SO^{2-}_4) by assuming the sum of all elements to 100 wt

% to allow internal standardization of the LA-ICP-MS data. If the vapor phase of HLIs that was filled by water approximated 10 vol % and possible up to 30 vol %, a salinity of 100 wt % salt can be overestimated less than 10 to 30%, which is accepted for spot analyses of inclusions. For the presented inclusion data, cationic and anionic (Cl^- and SO^{2-}_4) electrical charge balance is ≤0.2 mole (table S3), which reasonably consider the analytical uncertainties, especially the relatively large uncertainties of Cl and S analyzed by LA-ICP-MS, and the possibly presence of other anionic species, such as F^-, that we cannot directly measure for.

Sensitive high-resolution ion-microprobe (SHRIMP) oxygen isotopes

Zircon oxygen isotope analyses were performed using the SHRIMP II at RSES, ANU. The instrument conditions and analytical protocols are described in previous work (*68*) and are briefly summarized here. The primary Cs+ ion beam was accelerated at 15 keV with an intensity of 15 nA and burn time of 90 s. The ^{16}O and ^{18}O ion intensities were simultaneously measured by two Faraday caps. The values of $\delta^{18}O$ were standardized to Vienna Standard Mean Ocean Water compositions and corrected for the instrumental mass fractionation factor. FC-1 zircon (5.61 ± 0.14‰) was used as primary standard, and Mud Tank (5.03 ± 0.20‰), Plešovice (8.19 ± 0.08‰), and Temora 2 (8.20 ± 0.02‰) zircons were used as secondary standards (*69*, *70*). The reproducibility (external precision) of $\delta^{18}O$ is typically better than ±0.65‰ (2σ), and bias (accuracy) is less than ±0.40‰.

Supplementary Materials

This PDF file includes:
Supplementary Text
Figs. S1 to S10
Table S1 to S4
Legends for data S1 and S2
References

Other Supplementary Material for this manuscript includes the following:
Data S1 and S2

REFERENCES AND NOTES

1. Ningwu Research Group, *Ningwu Porphyry Iron Ores* (Geol. Publishing House, Beijing, 1978).
2. R. S. Hildebrand, Kiruna-type deposits; Their origin and relationship to intermediate subvolcanic plutons in the Great Bear magmatic zone, Northwest Canada. *Econ. Geol.* **81**, 640–659 (1986).
3. J. Mao, G. Xie, C. Duan, F. Pirajno, D. Ishiyama, Y. Chen, A tectono-genetic model for porphyry-skarn-stratabound Cu-Au-Mo-Fe and magnetite-apatite deposits along the Middle-Lower Yangtze River Valley, Eastern China. *Ore Geol. Rev.* **43**, 294–314 (2011).
4. J. Yu, Y. Chen, J. Mao, F. Pirajno, C. Duan, Review of geology, alteration and origin of iron oxide-apatite deposits in the Cretaceous Ningwu basin, Lower Yangtze River Valley, Eastern China: Implications for ore genesis and geodynamic setting. *Ore Geol. Rev.* **43**, 170–181 (2011).
5. O. Martinsson, K. Billström, C. Broman, P. Weihed, C. Wanhainen, Metallogeny of the Northern Norrbotten Ore Province, northern Fennoscandian Shield with emphasis on IOCG and apatite-iron ore deposits. *Ore Geol. Rev.* **78**, 447–492 (2016).
6. M. Reich, A. C. Simon, F. Barra, G. Palma, T. Hou, L. D. Bilenker, Formation of iron oxide-apatite deposits. *Nat. Rev. Earth Environ.* **3**, 758–775 (2022).
7. M. W. Hitzman, N. Oreskes, M. T. Einaudi, Geological characteristics and tectonic setting of Proterozoic iron oxide (Cu U Au REE) deposits. *Precambrian Res.* **58**, 241–287 (1992).
8. F. Tornos, F. Velasco, J. M. Hanchar, Iron-rich melts, magmatic magnetite, and superheated hydrothermal systems: The El Laco deposit, Chile. *Geology* **44**, 427–430 (2016).
9. A. H. Hofstra, C. J. Meighan, X. Song, I. Samson, E. E. Marsh, H. A. Lowers, P. Emsbo, A. G. Hunt, Mineral thermometry and fluid inclusion studies of the Pea Ridge iron oxide-apatite-rare earth element deposit, Mesoproterozoic St. Francois Mountains Terrane, southeast Missouri, USA. *Econ. Geol.* **111**, 1985–2016 (2016).
10. V. R. Troll, F. A. Weis, E. Jonsson, U. B. Andersson, S. A. Majidi, K. Högdahl, C. Harris, M.-A. Millet, S. S. Chinnasamy, E. Kooijman, K. P. Nilsson, Global Fe-O isotope correlation reveals magmatic origin of Kiruna-type apatite-iron-oxide ores. *Nat. Commun.* **10**, 1712 (2019).
11. A. A. Bookstrom, The magnetite deposits of El Romeral, Chile. *Econ. Geol.* **72**, 1101–1130 (1977).
12. M. D. Barton, D. A. Johnson, Evaporitic-source model for igneous-related Fe oxide-(REE-Cu-Au-U) mineralization. *Geology* **24**, 259–262 (1996).
13. J. L. Knipping, L. D. Bilenker, A. C. Simon, M. Reich, F. Barra, A. P. Deditius, M. Wälle, C. A. Heinrich, F. Holtz, R. Munizaga, Trace elements in magnetite from massive iron oxide-apatite deposits indicate a combined formation by igneous and magmatic-hydrothermal processes. *Geochim. Cosmochim. Acta* **171**, 15–38 (2015).
14. L. Corriveau, J.-F. Montreuil, E. G. Potter, Alteration facies linkages among iron oxide copper-gold, iron oxide-apatite, and affiliated deposits in the Great Bear magmatic zone, Northwest Territories, Canada. *Econ. Geol.* **111**, 2045–2072 (2016).
15. J. T. Ovalle, N. L. La Cruz, M. Reich, F. Barra, A. C. Simon, B. A. Konecke, M. A. Rodriguez-Mustafa, A. P. Deditius, T. M. Childress, D. Morata, Formation of massive iron deposits linked to explosive volcanic eruptions. *Sci. Rep.* **8**, 14855 (2018).
16. J. T. Ovalle, M. Reich, F. Barra, A. C. Simon, A. P. Deditius, M. Le Vaillant, O. K. Neill, G. Palma, R. Romero, N. Román, N. L. La Cruz, M. P. Roberts, D. Morata, Magmatic-hydrothermal evolution of the El Laco iron deposit revealed by trace element geochemistry and high-resolution chemical mapping of magnetite assemblages. *Geochim. Cosmochim. Acta* **330**, 230–257 (2022).
17. L.-P. Zeng, X.-F. Zhao, C. Spandler, H. Hu, B. Hu, J.-W. Li, Y. Hu, Origin of high-Ti magnetite in magmatic-hydrothermal systems: Evidence from iron oxide-apatite (IOA) deposits of eastern China. *Econ. Geol.* **117**, 923–942 (2022).
18. T. Hou, B. Charlier, F. Holtz, I. Veksler, Z. Zhang, R. Thomas, O. Namur, Immiscible hydrous Fe-Ca-P melt and the origin of iron oxide-apatite ore deposits. *Nat. Commun.* **9**, 1415 (2018).
19. W. M. Bain, M. Steele-Macinnis, K. Li, L. Li, F. K. Mazdab, E. E. Marsh, A fundamental role of carbonate-sulfate melts in the formation of iron oxide-apatite deposits. *Nat. Geosci.* **13**, 751–757 (2020).
20. S. T. M. Peters, N. Alibabaie, A. Pack, S. J. McKibbin, D. Raeisi, N. Nayebi, F. Torab, T. Ireland, B. Lehmann, Triple oxygen isotope variations in magnetite from iron-oxide deposits, central Iran, record magmatic fluid interaction with evaporite and carbonate host rocks. *Geology* **48**, 211–215 (2020).
21. W. M. Bain, M. Steele-Macinnis, F. Tornos, J. M. Hanchar, E. C. Creaser, D. K. Pietruszka, Evidence for iron-rich sulfate melt during magnetite(–apatite) mineralization at El Laco, Chile. *Geology* **49**, 1044–1048 (2021).
22. X. Xu, W. M. Bain, F. Tornos, J. M. Hanchar, H. M. Lamadrid, B. Lehmann, X. Xu, J. A. Steadman, R. S. Bottrill, M. Soleymani, A. Rajabi, P. Li, X. Tan, S. Xu, A. J. Locock, M. Steele-MacInnis, Magnetite-apatite ores record widespread involvement of molten salts. *Geology*, 10.1130/G51887.1, (2024).
23. W. Li, A. Audétat, J. Zhang, The role of evaporites in the formation of magnetite-apatite deposits along the Middle and Lower Yangtze River, China: Evidence from LA-ICP-MS analysis of fluid inclusions. *Ore Geol. Rev.* **67**, 264–278 (2015).
24. K. E. Watts, C. N. Mercer, Zircon-hosted melt inclusion record of silicic magmatism in the Mesoproterozoic St. Francois Mountains terrane, Missouri: Origin of the Pea Ridge iron oxide-apatite-rare earth element deposit and implications for regional crustal pathways of mineralization. *Geochim. Cosmochim. Acta* **272**, 54–77 (2020).
25. D. K. Pietruszka, J. M. Hanchar, F. Tornos, R. Wirth, N. A. Graham, K. P. Severin, F. Velasco, M. Steele-Macinnis, W. M. Bain, Magmatic immiscibility and the origin of magnetite-(apatite) iron deposits. *Nat. Commun.* **14**, 8424 (2023).
26. E. Roedder, Fluid Inclusions in *An Introduction to Studies of all Types of Fluid Inclusions, Gas, Liquid, or Melt, Trapped in Materials from Earth and Space* (Mineral. Assoc. Am., Washington, D.C., 1984), pp.1–644.
27. J. J. Wilkinson, Fluid inclusions in hydrothermal ore deposits. *Lithos* **55**, 229–272 (2001).
28. J. D. Webster, The exsolution of magmatic hydrosaline chloride liquids. *Chem. Geol.* **210**, 33–48 (2004).
29. T. Driesner, C. A. Heinrich, The system H_2O-NaCl. Part I: Correlation formulae for phase relations in temperature-pressure-composition space from 0 to 1000°C, 0 to 5000 bar, and 0 to 1 X_{NaCl}. *Geochim. Cosmochim. Acta* **71**, 4880–4901 (2007).
30. P. Fulignati, V. S. Kamenetsky, P. Marianelli, A. Sbrana, T. P. Mernagh, Melt inclusion record of immiscibility between silicate, hydrosaline, and carbonate melts: Applications to skarn genesis at Mount Vesuvius. *Geology* **29**, 1043–1046 (2001).
31. I. V. Veksler, A. M. Dorfman, P. Dulski, V. S. Kamenetsky, L. V. Danyushevsky, T. Jeffries, D. B. Dingwell, Partitioning of elements between silicate melt and immiscible fluoride, chloride, carbonate, phosphate and sulfate melts, with implications to the origin of natrocarbonatite. *Geochim. Cosmochim. Acta* **79**, 20–40 (2012).
32. C. Broman, J. O. Nyström, F. Henríquez, M. Elfman, Fluid inclusions in magnetite-apatite ore from a cooling magmatic system at El Laco, Chile. *GFF* **121**, 253–267 (1999).

33. P. Koděra, C. A. Heinrich, M. Wälle, J. Lexa, Magmatic salt melt and vapor: Extreme fluids forming porphyry gold deposits in shallow subvolcanic settings. *Geology* **42**, 495–498 (2014).
34. B. Rottier, K. Kouzmanov, A.-S. Bouvier, L. P. Baumgartner, M. Wälle, H. Rezeau, R. Bendezú, L. Fontboté, Heterogeneous melt and hypersaline liquid inclusions in shallow porphyry type mineralization as markers of the magmatic-hydrothermal transition (Cerro de Pasco district, Peru). *Chem. Geol.* **447**, 93–116 (2016).
35. W. Li, G. Xie, J. Mao, Q. Zhu, J. Zheng, Mineralogy, fluid inclusion, and stable isotope studies of the Chengchao deposit, Hubei Province, Eastern China: Implications for the formation of high-grade Fe skarn deposits. *Econ. Geol.* **114**, 325–352 (2019).
36. T. P. Mernagh, J. Mavrogenes, Significance of high temperature fluids and melts in the Grasberg porphyry copper-gold deposit. *Chem. Geol.* **508**, 210–224 (2019).
37. Z. Liu, X. Yang, C. Liu, D. Huang, W. Zhou, X. Teng, E. Liang, T. Dai, Genesis of Early Cretaceous porphyrite-type iron deposits and related sub-volcanic rocks in the Ningwu Volcanic Basin, Middle-Lower Yangtze Metallogenic Belt, Southeast China. *Int. Geol. Rev.* **60**, 1507–1528 (2018).
38. Y. Liu, Y. Fan, T. Zhou, L. Zhang, N. C. White, H. Hong, W. Zhang, LA-ICP-MS titanite U-Pb dating and mineral chemistry of the Luohe magnetite-apatite (MA)-type deposit in the Lu-Zong volcanic basin, Eastern China. *Ore Geol. Rev.* **92**, 284–296 (2018).
39. L.-P. Zeng, X.-F. Zhao, X.-C. Li, H. Hu, C. McFarlane, In situ elemental and isotopic analysis of fluorapatite from the Taocun magnetite-apatite deposit, Eastern China: Constraints on fluid metasomatism. *Am. Mineral.* **101**, 2468–2483 (2016).
40. R. H. Goldstein, T. J. Reynolds, *Systematics of Fluid Inclusions in Diagenetic Minerals* (SEPM Soci. Sediment. Geol. Short Course, 1994), p. 199.
41. R. J. Bodnar, O. M. Vityk, "Interpretation of microthermometric data for H_2O-NaCl fluid inclusions" in *Fluid Inclusions in Minerals: Methods and Applications.* (Virginia Tech University, Blacksburg, 1994), pp. 117–130.
42. A. Putnis, Mineral replacement reactions. *Rev. Mineral. Geochem.* **70**, 87–124 (2009).
43. J. C. Ayers, L. Zhang, Y. Luo, T. J. Peters, Zircon solubility in alkaline aqueous fluids at upper crustal conditions. *Geochim. Cosmochim. Acta* **96**, 18–28 (2012).
44. D. E. Harlov, R. Anczkiewicz, D. J. Dunkley, Metasomatic alteration of zircon at lower crustal P-T conditions utilizing alkali- and F-bearing fluids: Trace element incorporation, depletion, and resetting the zircon geochronometer. *Geochim. Cosmochim. Acta* **352**, 222–235 (2023).
45. L. Scholten, C. Schmidt, P. Lecumberri-Sanchez, M. Newville, A. Lanzirotti, M.-L. C. Sirbescu, M. Steele-Macinnis, Solubility and speciation of iron in hydrothermal fluids. *Geochim. Cosmochim. Acta* **252**, 126–143 (2019).
46. F. Ma, S. Jiang, Y. Jiang, P. Ni, H. Ling, Fluid inclusions and H-O isotopic compositions in the Washan and Dongshan iron deposits, Ningwu basin, China. *Acta Petrol. Sin.* **22**, 2581–2589 (2006).
47. A. E. Williams-Jones, I. M. Samson, K. M. Ault, J. E. Gagnon, B. J. Fryer, The genesis of distal zinc skarns: Evidence from the Mochito Deposit, Honduras. *Econ. Geol.* **105**, 1411–1440 (2010).
48. L. Mu, R. Hu, X. Bi, Y. Tang, T. Lan, Q. Lan, J. Zhu, J. Peng, A. Oyebamiji, New insights into the origin of the world-class Jinding sediment-hosted Zn-Pb deposit, southwestern China: Evidence from LA-ICP-MS analysis of individual fluid inclusions. *Econ. Geol.* **116**, 883–907 (2021).
49. H. P. Taylor, The application of oxygen and hydrogen isotope studies to problems of hydrothermal alteration and ore deposition. *Econ. Geol.* **69**, 843–883 (1974).
50. A. C. Harris, S. D. Golding, New evidence of magmatic-fluid-related phyllic alteration: Implications for the genesis of porphyry Cu deposits. *Geology* **30**, 335–338 (2002).
51. Z.-K. Su, X.-F. Zhao, L.-P. Zeng, K.-D. Zhao, A. H. Hofstra, Tourmaline boron and strontium isotope systematics reveal magmatic fluid pulses and external fluid influx in a giant iron oxide-apatite (IOA) deposit. *Geochim. Cosmochim. Acta* **259**, 233–252 (2019).
52. A. Audétat, A. C. Simon, "Magmatic controls on porphyry copper genesis" in *Geology and Genesis of Major Copper Deposits and Districts of the World: A Tribute to Richard H. Sillitoe.* (Soci. Econ. Geol., Littleton, 2012), pp. 553–572.
53. J. D. Webster, B. Goldoff, M. F. Sintoni, N. Shimizu, B. De Vivo, C-O-H-Cl-S-F volatile solubilities, partitioning, and mixing in phonolitic-trachytic melts and aqueous-carbonic vapor ± saline liquid at 200 MPa. *J. Petrol.* **55**, 2217–2248 (2014).
54. R. B. Symonds, W. I. Rose, T. M. Gerlach, P. H. Btiggs, R. S. Harmon, Evaluation of gases, condensates, and SO_2 emissions from Augustine volcano, Alaska: The degassing of a Cl-rich volcanic system. *Bull. Volcanol.* **52**, 355–374 (1990).
55. A. Afanasyev, J. Blundy, O. Melnik, S. Sparks, Formation of magmatic brine lenses via focussed fluid-flow beneath volcanoes. *Earth Planet. Sci. Lett.* **486**, 119–128 (2018).
56. G. Neusser, R. Abart, F. D. Fischer, D. Harlov, N. Norberg, Experimental Na/K exchange between alkali feldspar and an NaCl-KCl salt melt: Chemically induced fracturing and element partitioning. *Contrib. Mineral. Petrol.* **164**, 341–358 (2012).
57. P. Haseli, P. Majewski, F. Christo, M. Raven, S. Klose, F. Bruno, Experimental kinetic analysis of potassium extraction from ultrapotassic syenite using NaCl–$CaCl_2$ salt mixture. *ACS Omega* **5**, 16421–16429 (2020).
58. K. M. F. Almeida, D. M. Jenkins, Stability field of the Cl-rich scapolite marialite. *Am. Mineral.* **102**, 2484–2493 (2017).
59. D. A. Vanko, F. C. Bishop, Occurrence and origin of marialitic scapolite in the Humboldt Lopolith, N.W. Nevada. *Contrib. Mineral. Petrol.* **81**, 277–289 (1982).
60. S. R. Paterson, V. Memeti, R. Mundil, J. Žák, Repeated, multiscale, magmatic erosion and recycling in an upper-crustal pluton: Implications for magma chamber dynamics and magma volume estimates. *Am. Mineral.* **101**, 2176–2198 (2016).
61. A. Lundqvist, "The process water geochemistry of the Kiirunavaara ore", Licentiate Thesis, Luleå University of Technology (1998).
62. P. A. Rojas, F. Barra, M. Reich, A. Deditius, A. Simon, F. Uribe, R. Romero, M. Rojo, A genetic link between magnetite mineralization and diorite intrusion at the El Romeral iron oxide-apatite deposit, northern Chile. *Miner. Deposita* **53**, 947–966 (2018).
63. D. W. Haynes, K. C. Cross, R. T. Bills, M. H. Reed, Olympic Dam ore genesis: A fluid-mixing model. *Econ. Geol.* **90**, 281–307 (1995).
64. J. Hammerli, B. Rusk, C. Spandler, P. Emsbo, N. H. S. Oliver, In situ quantification of Br and Cl in minerals and fluid inclusions by LA-ICP-MS: A powerful tool to identify fluid sources. *Chem. Geol.* **337-338**, 75–87 (2013).
65. C. Paton, J. Hellstrom, B. Paul, J. Woodhead, J. Hergt, Iolite: Freeware for the visualisation and processing of mass spectrometric data. *J. Anal. At. Spectrom.* **26**, 2508–2518 (2011).
66. M. A. Kendrick, R. Arculus, P. Burnard, M. Honda, Quantifying brine assimilation by submarine magmas: Examples from the Galápagos Spreading Centre and Lau Basin. *Geochim. Cosmochim. Acta* **123**, 150–165 (2013).
67. M. Guillong, D. L. Meier, M. M. Allan, C. A. Heinrich, B. W. D. Yardley, P. J. Sylvester, SILLS: A MATLAB-based program for the reduction of laser ablation ICP-MS data of homogeneous materials and inclusions. *Mineral. Assoc. Canada Short Course Short Course Series* **40**, 328–333 (2008).
68. B. Fu, M. Bröcker, T. Ireland, P. Holden, L. P. J. Kinsley, Zircon U-Pb, O, and Hf isotopic constraints on Mesozoic magmatism in the Cyclades, Aegean Sea, Greece. *Int. J. Earth Sci.* **104**, 75–87 (2015).
69. L. P. Black, S. L. Kamo, C. M. Allen, D. W. Davis, J. N. Aleinikoff, J. W. Valley, R. Mundil, I. H. Campbell, R. J. Korsch, I. S. Williams, C. Foudoulis, Improved $^{206}Pb/^{238}U$ microprobe geochronology by the monitoring of a trace-element-related matrix effect; SHRIMP, ID-TIMS, ELA-ICP-MS and oxygen isotope documentation for a series of zircon standards. *Chem. Geol.* **205**, 115–140 (2004).
70. J. W. Valley, Oxygen isotopes in zircon. *Rev. Mineral. Geochem.* **53**, 343–385 (2003).
71. M. L. Frezzotti, F. Tecce, A. Casagli, Raman spectroscopy for fluid inclusion analysis. *J. Geochem. Explor.* **112**, 1–20 (2012).
72. F. H. Stewart, "Marine evaporites" in *Data of Geochemistry, sixth ed.* (US Government Printing Office, Washington, 1963). pp. 1–52.
73. S.-S. Sun, W. F. McDonough, Chemical and isotopic systematics of oceanic basalts: Implications for mantle composition and processes. *Geol. Soc. London Spec. Publ.* **42**, 313–345 (1989).
74. J. Veizer, J. Hoefs, The nature of O^{18}/O^{16} and C^{13}/C^{12} secular trends in sedimentary carbonate rocks. *Geochim. Cosmochim. Acta* **40**, 1387–1395 (1976).
75. D. P. Krylov, V. N. Zagnitko, S. Hoernes, I. P. Lugovaja, R. Hoffbauer, Oxygen isotope fractionation between zircon and water: Experimental determination and comparison with quartz-zircon calibrations. *Eur. J. Mineral.* **14**, 849–853 (2002).
76. L. D. Bilenker, A. C. Simon, M. Reich, C. C. Lundstrom, N. Gajos, I. Bindeman, F. Barra, R. Munizaga, Fe-O stable isotope pairs elucidate a high-temperature origin of Chilean iron oxide-apatite deposits. *Geochim. Cosmochim. Acta* **177**, 94–104 (2016).
77. O. Martinsson, R. L. Allen, O. Martinsson, P. Weihed, "Geology and metallogeny of the northern Norrbotten Fe-Cu-Au province" in *Svecofennian Ore-forming Environments: Volcanic-associated Zn-Cu-Au-Ag, Intrusion-Associated Cu-Au, Sediment-Hosted Pb-Zn, and Magnetite-Apatite Deposits in Northern Sweden of Northern Sweden* (Soci. Econ. Geol., Littleton, 2004), pp. 131–148.
78. J. B. H. Andersson, T. E. Bauer, O. Martinsson, Structural evolution of the Central Kiruna Area, Northern Norrbotten, Sweden: Implications on the geologic setting generating iron oxide-apatite and epigenetic iron and copper sulfides. *Econ. Geol.* **116**, 1981–2009 (2021).
79. D. S. Baker, Crystallization and alteration of quartz monzonite, Iron Springs mining district, Utah: Relation to associated iron deposits. *Econ. Geol.* **90**, 2197–2217 (1995).
80. Z. Bonyadi, G. J. Davidson, B. Mehrabi, S. Meffre, F. Ghazban, Significance of apatite REE depletion and monazite inclusions in the brecciated Se-Chahun iron oxide-apatite deposit, Bafq district, Iran: Insights from paragenesis and geochemistry. *Chem. Geol.* **281**, 253–269 (2011).

Acknowledgments: We thank X. Li, H. Hu, G. Wen, J. Chang, Z. Chang, Q. Shu, B. Rottier, B. Hu, K. Cao, V. S. Kamenetsky, and G. Chi for useful discussions and suggestions. We thank J. Wang, M. Rui, Z. Shi, D. Wang, and S. Chen for assistance in the field; J. Lu for the sample preparation; J.-M. Huizenga, Q. Xiong, and S. Cao for the Raman analyses; K. Blake and S. Askew for the CL imaging; and H. Huang for the trace element analyses of zircon. **Funding:** This work was supported by National Key Research and Development Program of China (2023YFF0804200), National Natural Research Foundation of China (41822203, 41972074, 42103064, and 42321001), and a fellowship from China Postdoctoral Science Foundation (2022M712951).

Author contributions: Conceptualization: X.-F.Z., L.-P.Z., C.S., J.M., J.-W.L., W.L., and Y.-Z.F. Methodology: X.-F.Z., L.-P.Z., J.M., T.P.M., J.-W.L., Y.H., W.L., and Y.-Z.F. Investigation: L.-P.Z., J.M., T.P.M., Y.H., Y.-Z.F., W.L., X.-F.Z., B.F., and J.-W.L. Resources: X.-F.Z., L.-P.Z., W.L., and Y.H. Funding acquisition: X.-F.Z., J.-W.L., L.-P.Z., and W.L. Data curation: X.-F.Z., B.F., and W.L. Validation: X.-F.Z., L.-P.Z., T.P.M., Y.H., W.L., Y.-Z.F., and J.-W.L. Supervision: X.-F.Z., J.M., J.-W.L., L.-P.Z., and W.L. Formal analysis: X.-F.Z., L.-P.Z., W.L., and Y.-Z.F. Project administration: X.-F.Z., L.-P.Z., J.M., J.-W.L., and W.L. Visualization: L.-P.Z., X.-F.Z., J.M., T.P.M., W.L., and J.-W.L. Writing–original draft: L.-P.Z., X.-F.Z., W.L., Y.-Z.F., and J.M. Writing–review and editing: L.-P.Z., X.-F.Z., C.S., J.M., T.P.M., W.L., and J.-W.L.

Competing interests: The authors declare that they have no competing interests. **Data and materials availability:** All data needed to evaluate the conclusions in the paper are present in the paper and/or the Supplementary Materials.

Submitted 18 August 2023
Accepted 22 March 2024
Published 24 April 2024
10.1126/sciadv.adk2174